Journal of Alloys and Compounds 509 (2011) 3326–3337

Contents lists available at ScienceDirect

Journal of Alloys and Compounds

journal homepage: www.elsevier.com/locate/jallcom

Phase formation in Mg–Sn–Si and Mg–Sn–Si–Ca alloys

A. Kozlov, J. Gröbner, R. Schmid-Fetzer*

Institute of Metallurgy, Clausthal University of Technology, Robert-Koch-Str. 42, D-38678 Clausthal-Zellerfeld, Germany

ARTICLE INFO

Article history:
Received 1 July 2010
Received in revised form 8 December 2010
Accepted 8 December 2010
Available online 15 December 2010

Keywords:
Microstructure
Magnesium alloys
Phase equilibria
Calphad modeling

ABSTRACT

Experimental work is done and combined with the Calphad method to generate a consistent thermodynamic description of the Mg–Ca–Si–Sn quaternary system, validated for Mg-rich alloys. The viability of a procedure for the selection of multicomponent key samples is demonstrated for this multicomponent system. Dedicated thermal analysis with DTA/DSC on sealed samples is performed and the microstructure of slowly solidified alloys is analyzed using SEM/EDX. The thermodynamic description and phase diagram of the ternary Mg–Si–Sn system, developed in detail also in this work, deviates significantly from a previous literature proposal. The phase formation in ternary and quaternary alloys is analyzed using the tool of thermodynamic equilibrium and Scheil calculations for the solidification paths and compared with present experimental data. The significant ternary/quaternary solid solubilities of pertinent intermetallic phases are quantitatively introduced in the quaternary Mg–Ca–Si–Sn phase diagram and validated by experimental data.

1. Introduction

Magnesium based Mg–Sn alloy systems recently attracted interest because of their potentially good mechanical properties at high temperatures [1]. Mg–Sn–Ca (TX) alloys are attractive candidates among Al-free alloys, potentially providing reasonable corrosion and good creep resistance [2–5]. It was shown that such alloys were able to compete with AZ91 in terms of corrosion behaviour and also showed a dramatic improvement of creep properties, comparable to the creep resistant alloy AE42 [6]. Interesting variations of these TX alloys require knowledge about the impact of other alloying elements such as Si and Ce in the corresponding multicomponent Mg-alloy systems TXS and TXE. All these new Al-free alloys enable the use of Zr as grain refiner, which is not possible in alloys of the AZ and AM group because of detrimental Al–Zr compound formation. The knowledge of the phase diagram and especially the consistent thermodynamic modeling of the Mg–Ca–Si–Sn system are prerequisite for a better understanding of alloy behaviour, aiming at focused alloy development and microstructure design during solidification and potential heat treatment.

The global goal of this study is to generate a thermodynamic description of phase equilibria in the Mg–Ca–Si–Sn alloy system, experimentally validated with an emphasis on Mg-rich alloys. This work includes an extensive analysis of ternary Mg–Si–Sn alloys.

It is state of the art to utilize the Calphad method [7–9] for the generation of consistent thermodynamic descriptions of binary and higher order systems, including the phase diagram. For ternary and multicomponent phase diagrams the experimental database is often scarce and sometimes contradictory. It is obviously an extremely time- and cost-consuming process to elaborate such phase diagrams solely by experimental work over wide ranges of compositions and temperatures. It has been demonstrated that this effort could be drastically reduced by selecting a relatively small number of key experiments that are decisive for the thermodynamic description of the multicomponent system [10]. This powerful procedure for the multicomponent key sample selection is applied in the present study to generate a consistent thermodynamic description of the Mg–Ca–Si–Sn quaternary system by combination of thermodynamic modeling with these properly selected experimental investigations.

2. Thermodynamics and phase equilibria

2.1. Literature data

Reliable and mutually consistent thermodynamic data for the binary subsystems are the key prerequisites to perform any reasonable, even exploratory, calculations in the quaternary system. The data sets of all six binary edge systems were selected from literature, namely Mg–Ca [11], Mg–Si [12], Mg–Sn [13], Ca–Si [14], Ca–Sn [15], Si–Sn [16]. The Calphad modeling of the Mg–Sn system was reported in Ref. [13] with an error, which subsequently had been corrected in a private communication with these authors; the corrected thermodynamic parameters of Mg–Sn system are presented in [11]. These thermodynamic data sets and the resulting calculated phase diagrams are considered to be quite satisfactory.

---

* Corresponding author. Tel.: +49 5323 72 2150; fax: +49 5323 72 3120.
E-mail address: schmid-fetzer@tu-clausthal.de (R. Schmid-Fetzer).

0925-8388/$ – see front matter © 2010 Elsevier B.V. All rights reserved.
doi:10.1016/j.jallcom.2010.12.052

Phase equilibria of the ternary systems Mg–Ca–Sn [11] and Mg–Ca–Si [14] were previously investigated by a combination of experimental work and thermodynamic assessments in our group. Importantly, these ternary descriptions are based exactly on the binary subsystems from literature [11–16]. For the ternary Ca–Si–Sn system no published experimental investigation or thermodynamic study could be found. Information about phase diagram, ternary phases/solubilities or thermodynamic assessment of the ternary Ca–Si–Sn system is not available in the literature.

The ternary Mg–Si–Sn system is in the focus of the present study. A thermodynamic assessment has been published by Jung et al. [17], using modified quasichemical model, based on the experimental data of [18,19]. Published experimental phase diagram data in the Mg–Si–Sn system are limited to the Mg_2Sn–Mg_2Si pseudobinary section. Experimental phase diagram outside that section cannot be found in the literature. Phase relations in the Mg_2Sn–Mg_2Si section were first investigated using thermal analysis, lattice parameter and microhardness variations by Muntyanu et al. [18] and later by Nikitin et al. [19]. These two groups have subsequently used their published phase relations as a basis for measurements of other thermophysical properties [20] and [21,22].

The first critical evaluation of this system has been done by Ferro et al. [23], noting some disagreement between results of [18] and [19], namely melting temperatures of pure components, different extents of solid solubilities in the binary compounds and different compositions for the three phases involved in the invariant reaction L + Mg_2Si = Mg_2Sn. The solubility of Si in Mg_2Sn is reported essentially the same, 14 at.% Si [18] compared with 13.3 at.% Si [19]. However, the solubility of Sn in Mg_2Si at about 600 °C significantly differs, 4.4 at.% Sn [18] versus 13.3 at.% Sn [19]. By selecting the results of [18] as the basis, a thermodynamic assessment has been done by Jung et al. [17], who accepted the value of Sn-solubility in Mg_2Si as 4.4 at.% and value of Si solubility in Mg_2Sn as 14 at.% Si. The thermodynamic assessment of [17] was subsequently used by the same authors in an interesting study of alloy design of Mg–Sn–Al–Si–(Sb–Zn–Mn) alloys [1]. Mg–Sn based alloys with additions of AZ31 alloy (and Si, Sb) were used in this investigation and therefore common elements such as Al, Zn and Mn are also contained in Mg–Sn based alloys. The SEM/EDS analysis of an as-cast TAS-sample, composition Mg–7.79Sn–2.73Al–0.70Si–0.69Zn–0.19Mn (wt.%), shows that the solubility of Si or Sn in binary Mg_2Sn and Mg_2Si phases is relatively low; values reported are about 3 at.% Si in Mg_2Sn and about 2 at.% Sn in Mg_2Si [1]. In that experimental paper some Mg–Si–Sn phase diagrams, calculated from the previous thermodynamic assessment of [17], are also given.

A rather unexpected indication to question the large solid solubility in the Mg_2Sn–Mg_2Si system came from a study of the final stage of solidification in a secondary aluminum alloy W319 of typical composition Al–7.5Si–3.5Cu–0.3Mg–0.1Sn (wt.%) [24]. The significant segregation of tin during solidification manifests itself in tiny precipitates of Mg_2Sn and (Sn), however, this cannot be pictured accepting the same large solubility values as done by Jung et al. [17] – it results in simulated precipitation of Mg_2Si alone and termination of solidification way above the stability of (Sn) [25]. It was predicted that the simplest and most effective solution to calculate the approximate constitution of that as-cast aluminum alloys is to assume, tentatively, a much smaller mutual solid solubility of Mg_2Si and Mg_2Sn in ternary Mg–Si–Sn system. Furthermore, our preliminary experimental phase analysis results of slowly solidified quaternary Mg–Ca–Si–Sn samples showed much lower solubility of Si in Mg_2Sn phase, namely 3–4 at.% Si versus 14–at.% Si from [18] and 13.3 at. % Si from [19], and solubility of Sn in Mg_2Si phase is 7–8 at. % Sn versus 4.4 at.% Sn [18] and 13.3 at.% Sn [19]. These reasons prompted our focus on reinvestigation of the ternary Mg–Si–Sn system.

2.2. Development of the Mg–Si–Sn ternary and Mg–Ca–Si–Sn quaternary thermodynamic descriptions

The thermodynamic parameters of the constituent binary systems are taken from previous works [11–16].

The Gibbs energy function for the element i (i = Mg, Sn, Ca, Si) in the ϕ phase (solid or liquid) is described by the equation:

$$G_i^{0,\phi}(T) = a + bT + cT\ln T + dT^2 + eT^3 + fT^{-1} + gT^7 + hT^{-9}, \qquad (1)$$

The standard element reference (SER) state has been chosen, which is hcp for Mg, bct for Sn, and diamond for Si, which results in zero enthalpy of the element (i) at 298.15 K and 1 bar in this SER state. T is the absolute temperature. The Gibbs energy function of the element i in its SER phase, ϕ = SER, is often denoted as $GHSER_i$,

$$\mathrm{GHSER}_i = G_i^{0,\mathrm{SER}}(T) \qquad (2)$$

The Gibbs energy functions for Mg, Sn, Ca and Si are taken from the SGTE (Scientific Group Thermodata Europe) compilation by Dinsdale [26].

The solution phases hcp (Mg), fcc (αCa), bcc (βCa), bct (Sn) and diamond (Si) are described by the substitutional solution model.

$$G^{\phi} = \sum_i x_i \cdot G_i^{0,\phi} + RT\sum_i x_i \ln x_i + \sum_{i,j>i} x_i \cdot x_j \cdot \sum_{\nu} L_{i,j}^{\nu,\phi} \cdot \left(x_i - x_j\right)^{\nu}, \qquad (3)$$

where x_i (x_j) represents the mole fraction of element (i) (j), (with (i) (j) = Mg, Sn, Ca and Si), R is the gas constant (R = 8.3145 J/mol K) and $L_{i,j}^{\nu,\phi}$ is the Redlich–Kister parameter representing the interaction between elements (i) and (j) [27]. The short-range order in the liquid phase is described by the associate solution model, resulting in two additional liquid species (i), Mg_2Sn and Ca_2Sn, with the summation in Eq. (3) covering (i) (j) = Mg_2Sn, Ca_2Sn, Mg, Sn, Ca and Si [11]. The interaction parameters, $L_{i,j}^{\nu,\phi}$, may be linearly temperature dependent and is usually expressed as $L_{i,j}^{\nu,\phi} = A_{i,j}^{\nu,\phi} + B_{i,j}^{\nu,\phi} \cdot T$

The thermodynamic description of the ternary Mg–Si–Sn system is developed in this work. The two phases Mg_2Si and Mg_2Sn have same crystal structure (CaF_2 structure type, $cF12$ Pearson symbol) and therefore these two phases are described as one phase, Mg_2X. The results from SEM/EDX presented below show that no complete solubility exists between the two binary end members. The asymmetric solid state demixing is introduced in the description of Mg_2X using interaction parameters presented in Table 1. The labeling Mg_2X' and Mg_2X'' have been used to distinguish between Sn-rich and Si-rich phases in this work, respectively. The designation Mg_2X' indicates the Mg_2(Si,**Sn**) phase and Mg_2X'' indicates the Mg_2(**Si**,Sn) phase, where major species on sublattices are highlighted by bold face.

For the other two Mg-containing ternary systems, Mg–Ca–Sn and Mg–Ca–Si, the thermodynamic descriptions are taken from the literature [11] and [14], respectively. Considering the lack of any experimental data for the ternary Ca–Si–Sn system we have performed only extrapolative calculations from the binary subsystems. That means that the Gibbs energy functions of solution phases in the ternary Ca–Si–Sn, the liquid phase and terminal solid solution phases (Ca), (Si) and (Sn), are constructed from the binary functions without ternary interaction parameters, whereas the Gibbs energies of intermetallic compounds are taken from the values of the binary edge systems. This approximation is considered to be of little impact to the phase equilibria in the Mg-corner of quaternary Mg–Ca–Si–Sn system.

In the quaternary description limited quaternary solubilities were introduced in the description of CaMgSn and CaMgSi intermetallic phases. These phases possess the same crystal structure,

Table 1
Thermodynamic parameters for the Mg–Si–Sn and Mg–Ca–Si–Sn systems. Major species on sublattices are highlighted by bold face. The compound energies listed refer to additional metastable end members of the solid solution phases while other values are given in the subsystems listed in original publications [11–16].

Phase name	Model	Parameters in J/(mol formula unit)
Mg_2X	$(Mg)_{0.5}(Sn,Si)_{0.25}$	$L^{0,Mg_2X}_{Mg:Sn,Si} = +5000$ $L^{1,Mg_2X}_{Mg:Sn,Si} = +900$
CaMgSn	$(\mathbf{Ca},\mathbf{Mg})_1(Ca)_1(\mathbf{Sn},Si)_1$	$G^{0,MgSnCa}_{Mg:Ca:Si} = -165000 + 45\,T + G^{0,HCP}_{Mg} + G^{0,FCC}_{Ca} + G^{0,Diamand}_{Si}$ $G^{0,MgSnCa}_{Ca:Ca:Si} = -140000 + 45\,T + 2G^{0,FCC}_{Ca} + G^{0,Diamand}_{Si}$
CaMgSi	$(Ca,\mathbf{Mg})_1(\mathbf{Ca})_1(Sn,\mathbf{Si})_1$	$G^{0,MgSiCa}_{Ca:Ca:Sn} = -140000 + 50\,T + 2G^{0,FCC}_{Ca} + G^{0,BCT}_{Sn}$ $G^{0,MgSiCa}_{Mg:Ca:Sn} = -158000 + 45\,T + G^{0,HCP}_{Mg} + G^{0,FCC}_{Ca} + G^{0,BCT}_{Sn}$ $G^{0,MgSiCa}_{Mg:Ca:Sn,Si} = -40000$

with Co_2Si (ordered anti $PbCl_2$) structure type and Pearson symbol *oP*12, and, theoretically, should be modeled as the same phase. However, no continuous solid solubility was detected in the quaternary system but rather two-phase structures of CaMgSn + CaMgSi. Modeling that as spinodal demixing would be quite complicated and require also more experimental data. Therefore, for practical reasons, separate Gibbs energy functions were assigned to CaMgSn and CaMgSi.

As explained in [11], the binary Ca_2Sn phase possesses the ternary solubility which terminates at the CaMgSn composition and this phase was modeled with the three sublattices $(Ca,Mg)_1Ca_1Sn_1$. The ternary phase named CaMgSi was modeled by Gröbner et al. [14] also as three sublattice line-compound $(Ca,Mg)_1Ca_1Si_1$ to reflect the experimentally observed ternary solubilities. In the present study, taking into account measured quaternary solubilities in these ternary phases, these phases were modeled with three sublattices as $(Ca,Mg)_1(Ca)_1(Sn,Si)_1$. However, the two phases are distinguished by the major species on the sublattices, indicated by bold font: The phase named CaMgSn, modeled as $(\mathbf{Ca},\mathbf{Mg})_1(Ca)_1(\mathbf{Sn},Si)_1$ covers the solution range from Ca_2Sn to CaMgSn with a limited solubility of Si. The phase named CaMgSi, modeled as $(Ca,\mathbf{Mg})_1(\mathbf{Ca})_1(Sn,\mathbf{Si})_1$ indicates the ternary CaMgSi composition with limited solubilities of Sn and Ca. The software package Pandat 8 [28,29] is utilized for all calculations in this work. The thermodynamic parameters for the ternary and quaternary system optimized in this work are listed in Table 1.

3. Experimental details

Four samples have been prepared in the ternary Mg–Si–Sn system with compositions given in Table 2. Sample numbers reflect the Mg-alloying component notations for Sn (T), Si (S) and Ca (X). One Mg-rich sample, TS1, was selected to verify the Mg-rich invariant reaction and three samples are located on the Mg_2Sn–Mg_2Si section. In the quaternary system five Mg–Ca–Si–Sn key samples, see Table 3, were selected to assess the accuracy of the calculated invariant five-phase reactions involving both the liquid and the (Mg) phase and having an Mg-rich overall composition, following the procedure given by Janz et al. [10]. The samples were analyzed by metallographic analysis, scanning electron microscopy with energy-dispersive X-ray microanalysis (SEM/EDX), differential thermal analysis (DTA) and differential scanning calorimetry (DSC). The details of each experimental procedure are described below.

3.1. Sample preparation

The starting materials for preparation of alloy samples were Mg pieces (99.99 mass%, Alfa, Karlsruhe, Germany), Sn bar (99.999 mass%, Alfa, Karlsruhe, Germany), Ca granules (99.99 mass%, Alfa, Karlsruhe, Germany) and Si chips (99.9998 mass%, Wacker, Burghausen, Germany). The pure elements were weighed, pressed into pellets, in order to break any oxide layers, and placed in a thin-walled tantalum capsule designed as a small cylinder with two ends. The second end was arc welded onto the filled Ta capsule under 1 bar argon atmosphere. This reduces the possibility of sample contamination, oxidation or loss due to vaporization, thus enabling repeated heating and cooling cycles [30]. All samples were then pre-melted in an evacuated test oven to allow alloy formation to occur and to check if the weld on the Ta capsule was secure before performing the high temperature DSC/DTA experiments. In the pre-melting cycle the capsule was heated at 10 K/min up to a temperature 100 K above the limit of the subsequent DSC/DTA experiments, which is in fact 200 K above the expected liquidus temperature of the sample. That temperature was held for 15 min allowing for a complete melting and alloying before cooling down at 10 K/min and taking the closed capsule to the DSC/DTA equipment. No inhomogeneity due to incomplete melting/alloying could be detected in any of the samples during the subsequent microstructure analysis.

3.2. DSC/DTA experiments

Thermal analyses by differential scanning calorimetry (DSC) and differential thermal analysis (DTA) were performed using a Setaram MHTC 96 DSC apparatus

Table 2
Temperatures extracted from the DTA/DSC signals obtained by thermal analysis in the Mg–Si–Sn system compared with data from thermodynamic calculation.

Nr.	Sample composition (at.%)	Thermal signal				Interpretation	
		Heating[a] (°C)		Cooling[b] (°C)		Calc. (°C)	Phase boundary or invariant reaction
TS1	Mg 90	630	w	–		632.4	$L/L + Mg_2X''$
	Sn 9.2	573	w	572	w	575.1	$L + Mg_2X''/L + Mg_2X'' + (Mg)$
	Si 0.8	566	s	563	s	562.9	$U_2: L + Mg_2X'' = Mg_2X' + (Mg)$
TS2	Mg 67	917	w	891	w	927.6	$L/L + Mg_2X''$
	Sn 25	826	w[c]	820	w[c]		
	Si 8	780	s[c]	787	s[c]	781.5	$m_1: L + Mg_2X'' = Mg_2X'$
		564	w	563	w	562.9	$U_2: L + Mg_2X'' = Mg_2X' + (Mg)$
TS3	Mg 66.7	967	s	950	s	969.4	$L/L + Mg_2X''$
	Sn 19.3	830	w[c]	819	w[c]		
	Si 14	782	s[c]	787	s[c]	781.5	$m_1: L + Mg_2X'' = Mg_2X'$
				628	w	634.7	$U_1: L + Mg_2X'' = Mg_2X' + (Si)$
TS4	Mg 66.7	978	s	965	s	985.6	$L/L + Mg_2X''$
	Sn 16.7	816	w[c]	827	w[c]		
	Si 16.6	783	s[c]	779	s[c]	781.5	$m_1: L + Mg_2X'' = Mg_2X'$

[a] Onset for invariant reactions, peak maximum otherwise.
[b] Onset (s = strong signal, w = weak and diffuse signal).
[c] Double signal, strong at the lower and weak at the higher temperature.

Table 3
Temperatures extracted from the DTA/DSC signals obtained by thermal analysis in the Mg–Ca–Si–Sn system compared with data from thermodynamic calculation.

Nr.	Sample composi-tion (at.%)	Thermal signal (°C) Heating[a]	Cooling[b]	Interpretation Calc. temperature	Phase boundary or invariant reaction
TXS1	Mg 87.329	745 w	735 w	769.0	$L/L + Mg_2X''$
	Ca 0.015	588 w	586 w	590.9	$L + Mg_2X''/L + Mg_2X'' + CaMgSn$
	Sn 9.896	–	–	564.7	$L + Mg_2X'' + CaMgSn/L + Mg_2X'' + CaMgSn + (Mg)$
	Si 2.76	564 s	563 s	562.8	U_5: $L + Mg_2X'' = CaMgSn + (Mg) + Mg_2X'$
TXS2	Mg 88.891	–	–	569.7	$L/L + Mg_2X''$
	Ca 0.01	–	–	565.1	$L + Mg_2X''/L + Mg_2\ X'' + Mg_2\ X''$
	Sn 10.764	564 s	563 s	562.8	U_5: $L + Mg_2X'' = CaMgSn + (Mg) + Mg_2X''$
	Si 0.335				
TXS3	Mg 90	892 w	890 w	922.5	$L/L + CaMgSi$
	Ca 7	–	–	861.6	$L + CaMgSi/L + CaMgSi + CaMgSn$
	Sn 2	624 s	624 s	605.2	$L + CaMgSi + CaMgSn/L + CaMgSi + CaMgSn + (Mg)$
	Si 1	519 s	518 s	515.4	U_6: $L + CaMgSi = CaMgSn + (Mg) + CaMg_2$
TXS4	Mg 90	914 w	910 w	918.5	$L/L + CaMgSn$
	Ca 4	648 w	640 w	658.2	$L + CaMgSn/L + CaMgSn + CaMgSi$
	Sn 5	621 s	619 s	633.3	$L + CaMgSi + CaMgSn/L + CaMgSi + CaMgSn + (Mg)$
	Si 1	[c]	[c]	589.3	U_4: $L + CaMgSi = (Mg) + Mg_2X'' + CaMgSn$
		564 w	563 w	562.8	Scheil: $U_5/L \rightarrow (Mg) + Mg_2X' + CaMgSn$
TXS5	Mg 90	849 w	843 w	889.0	$L/L + CaMgSn$
	Ca 2	–	–	646.8	$L + CaMgSn/L + CaMgSn + CaMgSi$
	Sn 7	[c]	[c]	604.1	$L + CaMgSi + CaMgSn/L + CaMgSi + CaMgSn + (Mg)$
	Si 1	603 s	600 s	589.3	U_4: $L + CaMgSi = (Mg) + Mg_2X'' + CaMgSn$
		565 s	563 s	562.8	U_5: $L + Mg_2X'' = CaMgSn + (Mg) + Mg_2X'$

[a] Onset for invariant reactions, peak maximum otherwise.
[b] Onset (s = strong signal, w = diffuse signal).
[c] See remarks in text.

(SETARAM Instrumentation, Caluire, France) and Netzsch DTA 404 S (NETZSCH-Gerätebau GmbH, Selb, Germany), respectively. For all samples, tests were run at ±5 K/min from about 100 K below to about 100 K above the expected reaction temperature, obtained from calculated phase diagrams based on preliminary datasets. These are essentially extrapolations from the binary and ternary subsystems. Each DSC/DTA experiment included three heating and cooling cycles, where the first heating cycle usually did not show reasonable results. No reactions between the samples and the Ta capsule were observed. There were also no signs of reaction between the outside of the Ta capsule and sample holder or protective gas used in the DSC/DTA apparatus. For the cooling curves, onset temperatures are determined. The heating peaks are interpreted according to the peak shape analysis; for invariant reactions, onset temperatures are determined and otherwise peak maximum temperatures are evaluated. Some signals were weak and diffuse as indicated with the tabulated results.

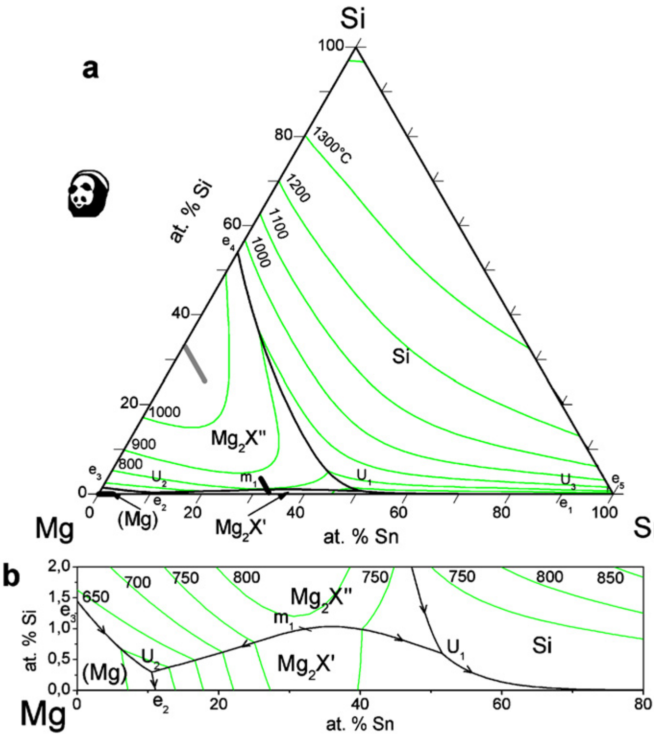

Fig. 1. (a) Calculated Mg–Si–Sn liquidus surface. The bold gray lines indicate the maximum solid solubilities in the pseudobinary section $Mg_2Si–Mg_2Sn$ at the invariant reaction $L + Mg_2X'' = Mg_2X'$. (b) Magnified Mg–Sn side. Mg_2X' indicates the Mg_2**Sn**-rich phase and Mg_2X'' indicates the Mg_2**Si**-rich phase.

3.3. SEM/EDX analysis

A CamScan 44 scanning electron microscope (Obducat CamScan, Cambridge) (SEM) was used to analyze the microstructure of the samples after solidification with slow (5 K/min) cooling rate in the final thermal analysis run. Back scattered electrons were used to produce the images shown in this publication while secondary electron images were used to help identify the difference between a darker phase and a depression or hole in the surface of the sample before conducting energy dispersive X-ray (EDX) analysis. For optimal resolution in the SEM the samples were embedded in electrically conductive material and polished to 1 μm.

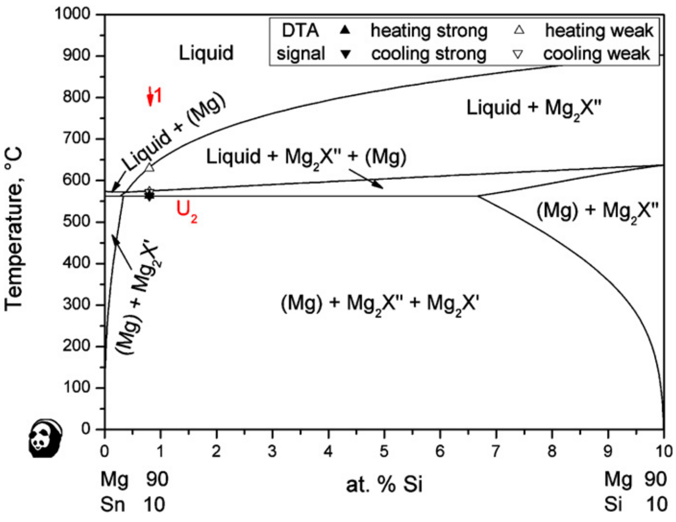

Fig. 2. Calculated vertical section of the Mg–Si–Sn phase diagram at 90 at.% Mg with thermal signals of sample TS1 measured in this work.

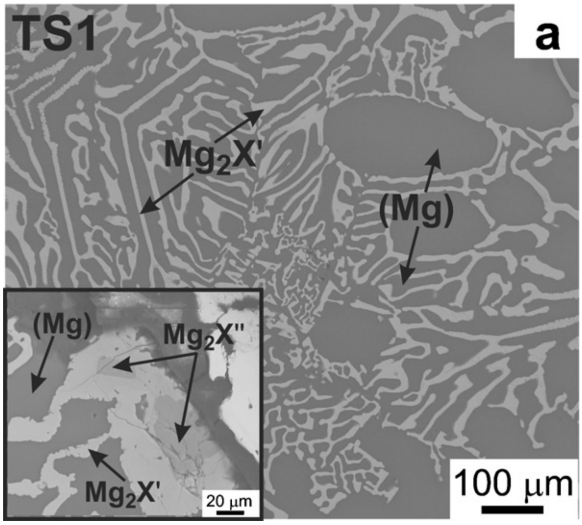

Fig. 3. SEM/BSE micrograph of sample TS1 after slow cooling.

4. Results and discussion

4.1. The ternary Mg–Si–Sn system

Results of the thermal analysis of the four samples investigated in this work are presented in Table 2. The thermal signals are evaluated from the three independent heating and cooling cycles for each sample. Strong and wide (double) peaks have been detected in region 780–830 °C in all three samples TS2–TS4 located on the Mg_2Sn–Mg_2Si section. This is the lower temperature value with the stronger part of these double peaks.

The interpretations of the experimental temperatures in the last column are based on the final thermodynamic calculation developed in this work. The calculated liquidus surface over the entire composition range is shown in Fig. 1 with a detailed view of the Mg–Sn-rich edge. From the present calculation, three invariant four-phase reactions and one invariant three-phase maximum involving the liquid phase are identified and compiled in Table 4. For the three Mg-richest reactions, m_1, U_1 and U_2, our experimental values, evaluated from Table 2, are shown for comparison in Table 4. The three last columns compile the literature data [17–19].

The calculated vertical phase diagram section at 90 at.% Mg with superimposed data from sample TS1 is presented in Fig. 2. Experimental literature data are not available. It is obvious that the thermal signals agree with the calculation, given more exactly in Table 2. The microstructure of this sample in Fig. 3 clearly shows in the magnified inset that Mg_2X'' precipitates before Mg_2X'. The larger grains of (Mg) correspond to a large amount of this phase, even a (Mg) dendrite is visible at the right hand side of Fig. 3. It is not clear from this microstructure if the very small amount of Mg_2X'' precipitates before (Mg) or vice versa. Finally, in an apparently eutectic-like structure, the (Mg) phase occurs jointly with Mg_2X'. The magnified inset also shows larger crystals of Mg_2X' around the primary Mg_2X''. That may be due to the fact that the primary Mg_2X'', having the same crystal structure, could provide potent nucleation sites for the growth of Mg_2X'.

This is in excellent agreement with the calculated phase fractions along the solidification path of sample TS1 under equilibrium condition given in Fig. 4a. After primary solidification of Mg_2X'' the secondary precipitation $L \rightarrow (Mg) + Mg_2X''$ produces significantly more (Mg). This is followed by the invariant transition-type reaction U_2: $L + Mg_2X'' = (Mg) + Mg_2X'$, however, the amount of consumed Mg_2X'' is negligible. That is why the occurrence of $(Mg) + Mg_2X'$ resembles a eutectic-like structure. This is also seen in Fig. 1b by the very small Si content of liquid at U_2, only 0.31 at.% Si, which makes U_2 almost degenerate to the binary Mg–Sn eutectic e_2.

Here we have a significant distinction to the phase diagram calculation by Jung et al. [17], showing a much wider primary crystallization field of (Mg), even though the temperature calculated for U_2 is similar. According to that calculation sample TS1 should have unambiguously produced primary (Mg) which is in distinct conflict with the experimental result and the present calculation.

It is interesting to note that the calculated Scheil solidification path (see Fig. 4b) for sample TS1 is almost identical to the equilibrium solidification path. Under Scheil condition the invariant reaction U_2 cannot proceed because of its transition-type, requiring consumption of Mg_2X''. It is overrun and the liquid solidifies along the very short monovariant reaction $L \rightarrow (Mg) + Mg_2X'$ between U_2 and e_2 in the temperature range 562.88–562.83 °C. Also, the amounts of solidified phases are virtually identical to the equilibrium case.

The calculated phase diagram along the exact composition section Mg_2Sn–Mg_2Si reveals a pseudobinary system. It is shown as solid lines in Fig. 5. The invariant three-phase reaction $L + Mg_2X'' = Mg_2X'$ at 781.5 °C is the calculated pseudobinary peritectic, denoted also as the maximum m_1 in Fig. 1 and Tables 2 and 4. Melting points of the pure compounds are 1081.4 °C (Mg_2Si) and

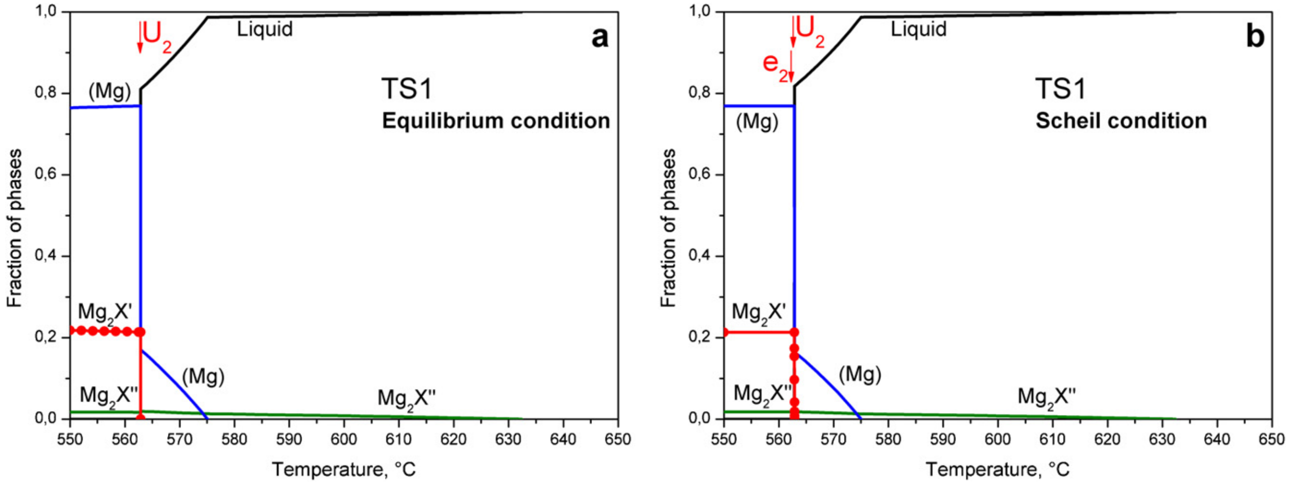

Fig. 4. Phase amounts for sample TS1, see Fig. 2, calculated for solidification under (a) equilibrium and (b) Scheil conditions. U_2 is a transition-type reaction, $L + Mg_2X'' = Mg_2X' + (Mg)$, and e_2 is the binary eutectic $L = Mg_2Sn + (Mg)$.

Table 4
Calculated invariant ternary reactions involving liquid phase in the Mg–Si–Sn system. Comparison of calculated and experimental data from this work with literature data.

Type	Invariant reaction	Temperature (°C)			Method	Reference
		Calc.[a]	Exp.[a]	Lit.		
m_1	$L + Mg_2X'' = Mg_2X'$	781.5	782	857855860	CalculationExperimentalExperimental	[17][18][19]
U_1	$L + Mg_2X'' = Mg_2X' + Si$	634.7	628	758	Calculation	[17]
U_2	$L + Mg_2X'' = (Mg) + Mg_2X'$	562.9	564	563	Calculation	[17]
U_3	$L + Si = Mg_2X' + Sn$	203.9		200	Calculation	[17]

[a] This work.

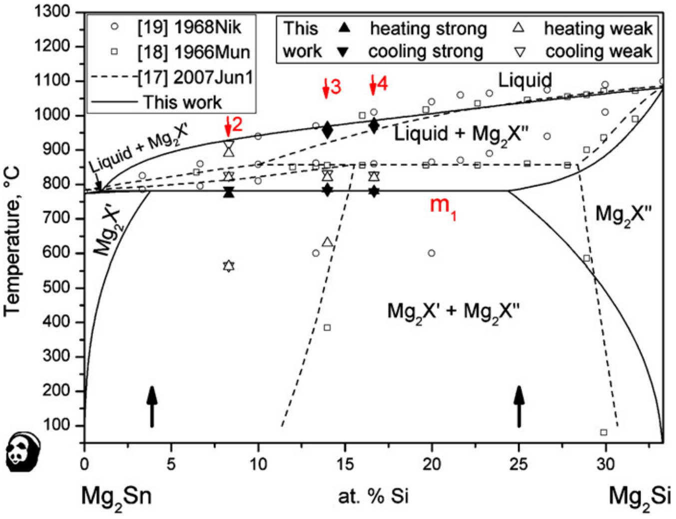

Fig. 5. Calculated pseudobinary Mg_2Sn–Mg_2Si section of the Mg–Si–Sn phase diagram (constant 66.6667 at.% Mg, solid lines). Thermal signals of samples TS2–TS4 measured in this work and experimental literature data [18,19] are superimposed, together with the calculated phase diagram of Jung et al. [17]. Mg_2X' indicates the Mg_2Sn-rich and Mg_2X'' the Mg_2Si-rich solid solution phase. Arrows plotted at low temperature indicate the measured solid solubilities in the present slowly cooled samples.

774.0 °C (Mg_2Sn). Superimposed in Fig. 5 are data from samples TS2 to TS4 and the available literature data. The key point is the conflicting data on the mutual solid solubilities among Mg_2X' and Mg_2X''.

The microstructure investigations and EDX analysis of all slowly (5 K/min) solidified samples (TS1–TS4) indicate solid solubilities of about 3–4 at.% Si in Mg_2X' and about 7–8 at.% Sn in Mg_2X''. These data are plotted in Fig. 5 as arrows since it is hard to assign a temperature value, however, a reasonable agreement with the present calculation may be suggested.

In comparison with literature data, first of all the huge discrepancy between the experimental solubility data of Sn in Mg_2X'' between Muntyanu et al. (4.4 at.% Sn) [18] and Nikitin et al. (13.3 at.% Sn) [19] at about 600 °C is emphasized. These data are plotted as the open square and the open circle, respectively, in Fig. 5. Since both authors used essentially the same experimental methods (thermal analysis, lattice parameter and microhardness variations) this casts some doubt on these values. Data for the solubility of Si in Mg_2X' from both groups are similar, 14 at.% Si [18] and 13.3 at.% Si [19] compared to the present 3–4 at.% Si.

It is noted that the smaller solid solubility values are also indicated by experimental investigations of a Mg-rich Mg–Sn–Al–Si–Zn–Mn alloy by Jung et al. [1] and the predicted final stage of solidification in a secondary aluminum alloy Al–7.5Si–3.5Cu–0.3Mg–0.1Sn (wt.%) by Emadi et al. and Schmid-Fetzer [24,25], as detailed in Section 2.1. The presently evaluated mutual solubilities are, however, corroborated by two stronger points, the thermal analysis data and the primary phases as detailed below.

The large solubility values of Si in Mg_2X' [18,19] are entirely incompatible with the pseudobinary peritectic temperature, at the invariant three-phase maximum m_1, $L + Mg_2X'' = Mg_2X'$, consistently measured in the present work as strong peaks very close to the calculated value of 781.5 °C. It is emphasized that these data, detailed in Table 2, are obtained by dedicated DTA/DSC experiments with multiple runs on samples sealed in Ta-capsules. By contrast, the thermal signals reported at 855 °C and 860 °C by Muntyanu et al. [18] and Nikitin et al. [19], respectively, for that invariant reaction have been obtained by inferior experimental procedures. Muntyanu et al. [18] used only one run with

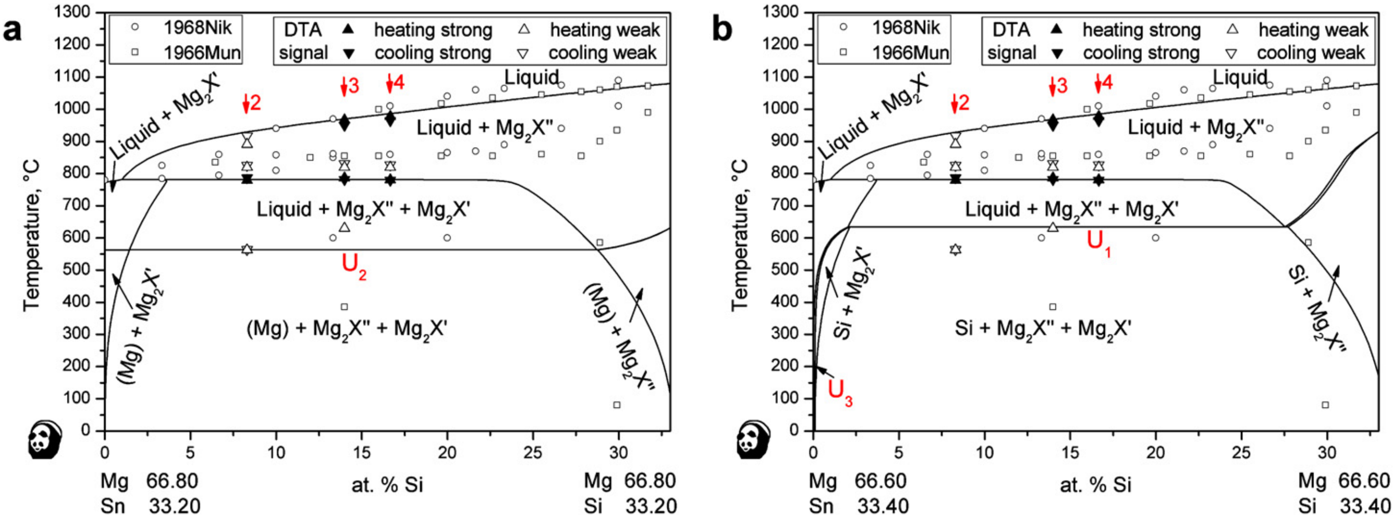

Fig. 6. Calculated vertical sections of the Mg–Si–Sn phase diagram at (a) 66.80 at.% Mg and (b) 66.60 at.% Mg. The superimposed experimental data are the same as in the exact pseudobinary section, Fig. 5.

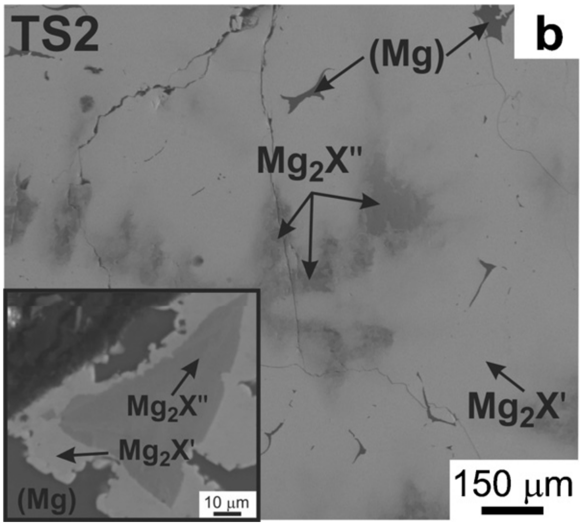

Fig. 7. SEM/BSE micrograph of sample TS2 after slow cooling.

15–20 K/min, sample molten in corundum crucibles in air; Nikitin et al. [19] used only one heating run with 1.5 K/min, sample molten in corundum crucibles in a steel container under argon. We were not able to reproduce these data in our more sophisticated experiments and did not observe any peak in the 840–870 °C temperature range on any DTA/DSC curve. Good agreement is observed in Fig. 5 between calculated and experimental results of the present investigations, especially for the strong and important thermal signals of the invariant reaction, but also for the liquidus data.

For samples TS2 and TS3 two weak peaks have been detected at 564 °C and 628 °C, respectively. These data are presented in Table 2 with the assigned interpretation. This cannot be understood in the exact pseudobinary section Mg_2X'–Mg_2X'' in Fig. 5. However, the picture changes when the sample composition is slightly shifted by weighing uncertainties in magnesium content away from Mg_2X'–Mg_2X'' section. This is exemplified in Fig. 6a for a constant magnesium composition of 66.80 at.% Mg. With this slight excess of Mg the invariant reaction U_2, $L + Mg_2X'' = Mg_2X' + (Mg)$, appears at 563 °C, in agreement with the weak thermal signal from sample TS2. In fact, a small amount of (Mg) from reaction U_2 appears in the microstructure of sample TS2 in Fig. 7, supporting this interpretation of the thermal signal. Reaction U_2 was also confirmed by the strong peak in sample TS1.

The microstructure of sample TS2, Fig. 7, also demonstrates that Mg_2X'' clearly is the primary phase, engulfed by Mg_2X' and that a sharp phase boundary is observed. This is an additional confirmation of the present interpretation of the strong thermal signal at the peritectic temperature m_1 in Fig. 5. Assuming the validity of the previous phase diagram, shown dashed, sample TS2 would have produced Mg_2X' as primary phase and no Mg_2X'' at all, in contradiction to the experimental observation.

In the slightly Mg-deficient section at constant 66.60 at.%, shown in Fig. 6b, the invariant reaction U_1, $L + Mg_2X'' = Mg_2X' + Si$, appears at 635 °C. This corresponds to the small DTA peak of sample TS3, thus validating this reaction temperature. In the microstructure of sample TS3, not shown here, the Si-phase cannot be found which is consistent with the calculated negligible amount of only 0.1% of this phase, formed under equilibrium condition. The comparison of all invariant temperatures in Table 4 indicates a reasonable agreement between the experimental value and the present calculation of the temperature of that invariant reaction U_1 and also the significant difference to the calculation by Jung et al. [17].

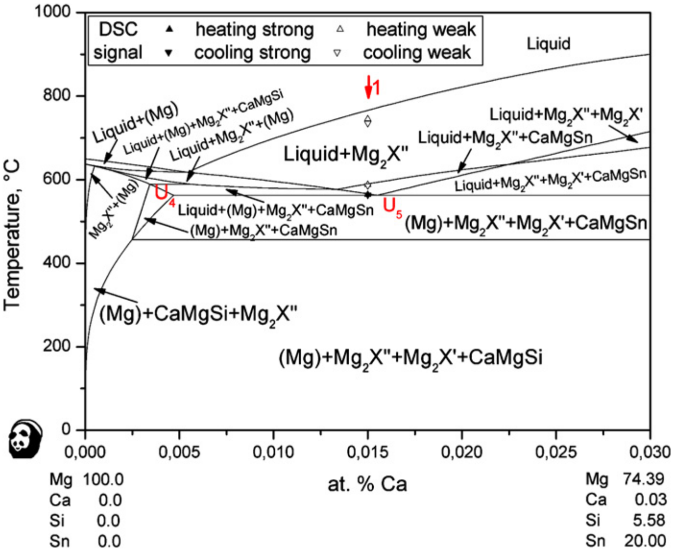

Fig. 8. Calculated vertical phase diagram section Mg–$Mg_{74.39}Ca_{0.03}Si_{5.58}Sn_{20}$ in the Mg–Ca–Si–Sn quaternary system compared with experimental data from DSC of sample TXS1.

4.2. Quaternary Mg–Ca–Si–Sn alloys

The compositions of the five Mg–Ca–Si–Sn key samples and the results of thermal measurements and their interpretation are summarized in Table 3. Using the algorithm presented in [10], two Mg–Ca–Si–Sn key samples were selected to assess the accuracy of the calculated invariant five-phase reactions involving both the liquid and the (Mg) phase and having a Mg-rich overall composition. Another three quaternary key samples were selected for investigation along the vertical section with 90 at.% of Mg. Both series of samples were selected based on preliminary thermodynamic calculation and having a Mg-rich overall composition more than 70 at.% of Mg to check invariant reaction U_4, U_5 and U_6 as shown in Table 5.

Two intermetallic phases are relevant in the quaternary system with quaternary composition and solubility ranges, designated here as CaMgSi and CaMgSn in a shorthand notation. CaMgSi originates from the end member of the ternary solid solution $Mg_{1-x}SiCa_{1+x}$ ($x = 0$–0.2) [14], while CaMgSn originates from the binary Ca_2Sn with a ternary solution range Mg_xSnCa_{2-x} ($x = 0$–1) [11]. In equilibrium with (Mg), that is for Mg-rich alloys, the shorthand notations CaMgSi and CaMgSn very closely reflect the compositions of these intermetallic phases in the ternary systems. In the quaternary samples, which are in equilibrium with (Mg), a solubility of Sn in CaMgSi and a solubility of Si in CaMgSn was discovered with solution ranges up to both, 10 at.% Sn and 10 at.% Si.

Fig. 8 shows a calculated phase diagram section from pure Mg through the composition of the first sample, TXS1, together with the thermal DSC signals. This sample validates the temperature of the invariant transformation U_5: $L + Mg_2X'' = CaMgSn + (Mg) + Mg_2X'$ at 563 °C, which it was selected for. A quite reasonable agreement is also found for the liquidus and the transition temperature to the three-phase region. This finding is corroborated by the phase assembly detected in the microstructure of the slowly cooled sample. The microstructure of the sample TXS1 in Fig. 9 clearly shows that Mg_2X'' is the primary crystallizing phase. It is engulfed by Mg_2X', which also appears jointly with (Mg) in a eutectic-like structure. Some CaMgSn is also found indicated in the enlarged inset in Fig. 9 as the very bright lamella, hard to see in this reproduction but clearly in the microscope. This is consistent with the calculated solidification path under equilibrium condition in Fig. 10a, showing

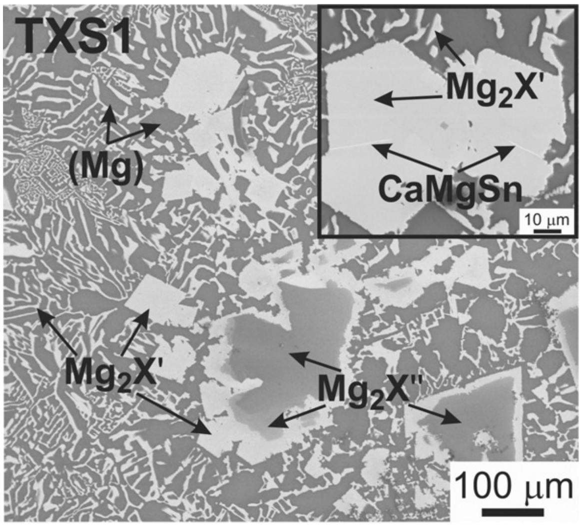

Fig. 9. Scanning electron micrograph (SEM/BSE) of sample TXS1 after slow cooling in DSC. The inset at top right shows a higher magnification of the Mg_2X' region where the fine white lamellae of CaMgSn are identified.

the termination of solidification in the reaction U_5 at 563 °C. Even though four solid phases are involved in this invariant reaction, essentially only (Mg) + Mg_2X' are formed in significant amount, explaining the eutectic-like structure. It is noteworthy that the calculated solidification path under Scheil conditions, given in Fig. 10b, is not much different even though all solid phases involved exhibit significant solid solubility. Reaction U_5 cannot take place in this case because of its transition-type, however, immediately after that point the solidification of the entire residual liquid occurs in the narrow range between about 562.83 and 562.77 °C in the reaction $L \rightarrow (Mg) + Mg_2X'$ ($+Mg_2X''$). Thus, the assumption of Scheil conditions would also be consistent with both, the essentially invariant appearance of the DSC signal and the observed microstructure.

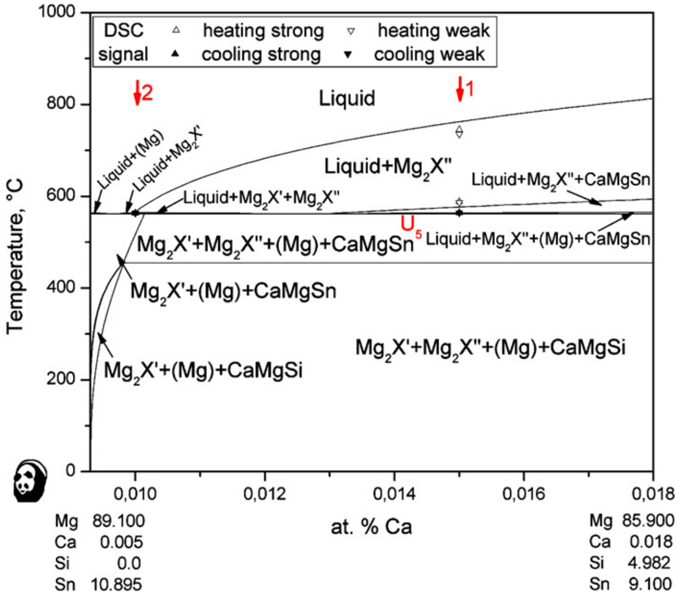

Fig. 11. Calculated vertical phase diagram section $Mg_{89.1}Ca_{0.005}Sn_{10.895}$–$Mg_{85.9}Ca_{0.018}Si_{4.982}Sn_{9.1}$ in the Mg–Ca–Si–Sn quaternary system compared with experimental data from DSC of samples TXS1 and TXS2.

Fig. 11 shows the calculated phase diagram section through the composition of the two Ca-poor key samples, TXS1 and TXS2, together with the thermal DSC signals. For sample TXS1 this provides just a different view on the same phase equilibria discussed above.

The microstructure of sample TXS2 in Fig. 12 shows only two phases, Mg_2X' and (Mg), even though the phase diagram

Table 5
Calculated invariant reactions and liquid phase compositions in the Mg-corner of the Mg–Ca–Si–Sn system compared with measured temperatures, this work.

Type	Reaction	Liquid composition, (at.%)				Temperature (°C)	
		Mg	Ca	Si	Sn	Calc.	Exp.
U_1	$L + Ca_7Mg_6Si_{14} + CaMgSi = CaMgSn + Mg_2X''$	66.85	2.04	16.62	14.49	985.1	–
U_2	$L + CaMgSn + Mg_2X'' = Mg_2X' + Ca_7Mg_6Si_{14}$	56.86	3.29	0.55	39.30	754.0	–
U_3	$L + CaMgSi = CaMgSn + Ca_2Si + CaMg_2$	61.33	36.91	0.03	1.73	700.2	–
U_4	$L + CaMgSi = (Mg) + Mg_2X'' + CaMgSn$	91.86	0.02	0.56	7.56	589.3	603
U_5	$L + Mg_2X'' = CaMgSn + (Mg) + Mg_2X'$	89.06	0.01	0.31	10.62	562.8	564
U_6	$L + CaMgSi = CaMgSn + (Mg) + CaMg_2$	88.93	10.87	1×10^{-6}	0.2	515.4	518

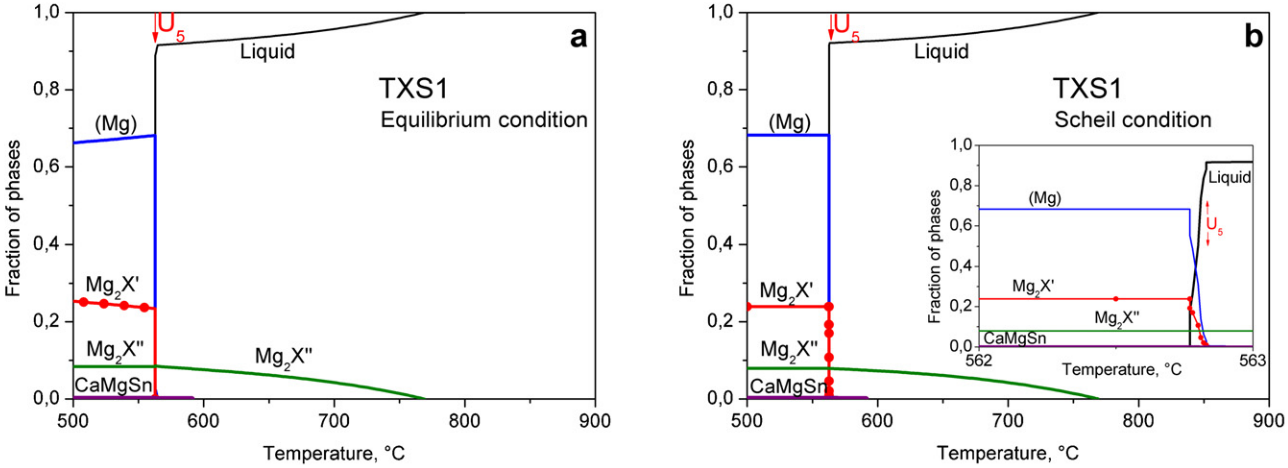

Fig. 10. Phase amounts for sample TXS1, see Fig. 8, calculated for solidification under (a) equilibrium and (b) Scheil conditions.

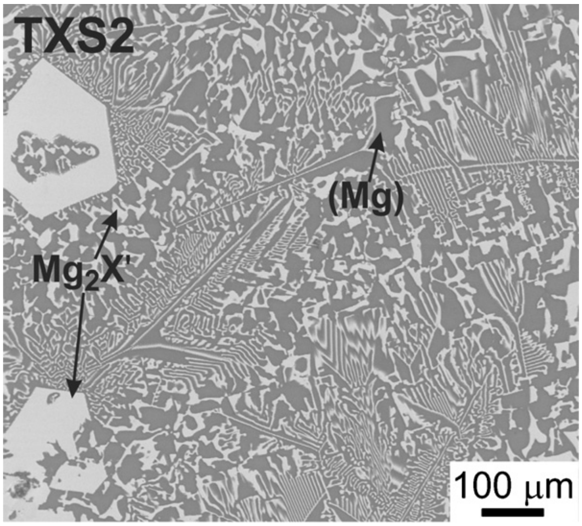

Fig. 12. Scanning electron micrographs (SEM/BSE) of sample TXS2 after slow cooling in DSC.

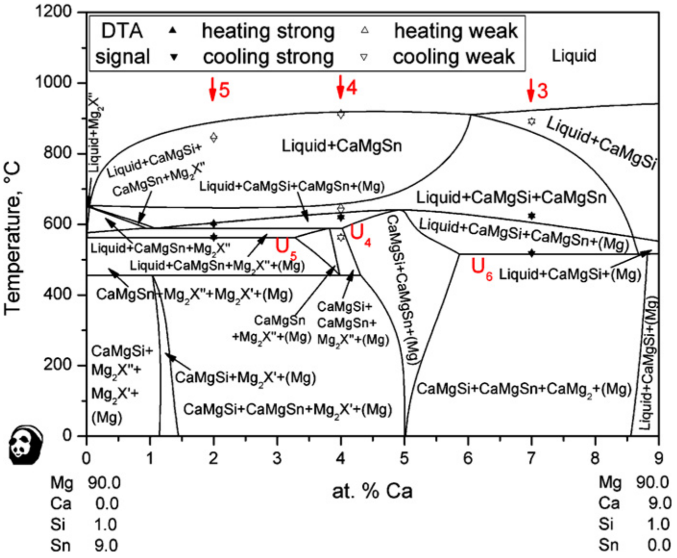

Fig. 14. Calculated vertical phase diagram section in the Mg–Ca–Si–Sn quaternary system $Mg_{90}Si_1Sn_9$–$Mg_{90}Ca_9Si_1$. The experimental thermal analysis data from DSC for samples TXS3, TXS4 and TXS5 are superimposed.

in Fig. 11 indicates Mg_2X'' to be the primary phase. This apparent contradiction is resolved by the calculated phase fractions during equilibrium solidification in Fig. 13a. Indeed, Mg_2X'' crystallizes as primary phase at 570 °C, but in a negligible fraction with a maximum of only 0.0007 at 565 °C where Mg_2X' starts to form. Therefore, only very little liquid solidifies in the reaction U_5, $L + Mg_2X'' = CaMgSn + (Mg) + Mg_2X'$ at 562.8 °C, since almost no Mg_2X'' is available. Solidification occurs essentially in the narrow temperature range 562.83–562.80 °C by $L \rightarrow (Mg) + Mg_2X'$ (+CaMgSn), which nicely explains the apparently eutectic-like microstructure in the main part of Fig. 12. Similar to the ternary sample TS1 in Fig. 3, the larger crystals of Mg_2X' might be due to the fact that some Mg_2X'' had already solidified before, thus providing potent nucleation sites for the growth of Mg_2X'. Again, the comparison of the equilibrium case with calculated phase fractions under Scheil conditions in Fig. 13b indicates essentially the same solidification path. The main solidification range is just extended to a slightly lower temperature of 562.77 °C and in both cases the calculated fraction of CaMgSn is below 0.0003, not detectable in the microstructure.

The three samples TXS3 to TXS5 are all located on the 90 at.% Mg section and that calculated vertical phase diagram sectionis shown in Fig. 14 together with the thermal signals from these samples. More details on the phase diagram are given in the next section.

The present equilibrium calculation demonstrates that sample TXS3 solidifies primary CaMgSi between 922 °C and 861 °C, followed by secondary precipitation of CaMgSn, third precipitation of (Mg) until solidification terminates in the invariant reaction U_6, $L + CaMgSi = CaMgSn + (Mg) + CaMg_2$ at 515 °C. The microstructure of this sample in Fig. 15a shows good agreement with this calculated phase formation, which is additionally supported by the agreement with the DTA signals, especially for the quaternary invariant reaction U_6.

The microstructures of both samples TXS4 and TXS5 in Fig. 15b and c, respectively, clearly show a significant amount of primary CaMgSn phase, in agreement with the calculation. The secondary CaMgSi precipitation, seen in the phase diagram section, produces only negligible phase fractions in contrast to the following phase field with calculated huge amounts of (Mg), again in agreement with the microstructures.

In sample TXS5 the subsequent solidification of Mg_2X'' and Mg_2X' occurs at invariant reactions in agreement with the strong thermal signals given in Table 3 and also depicted

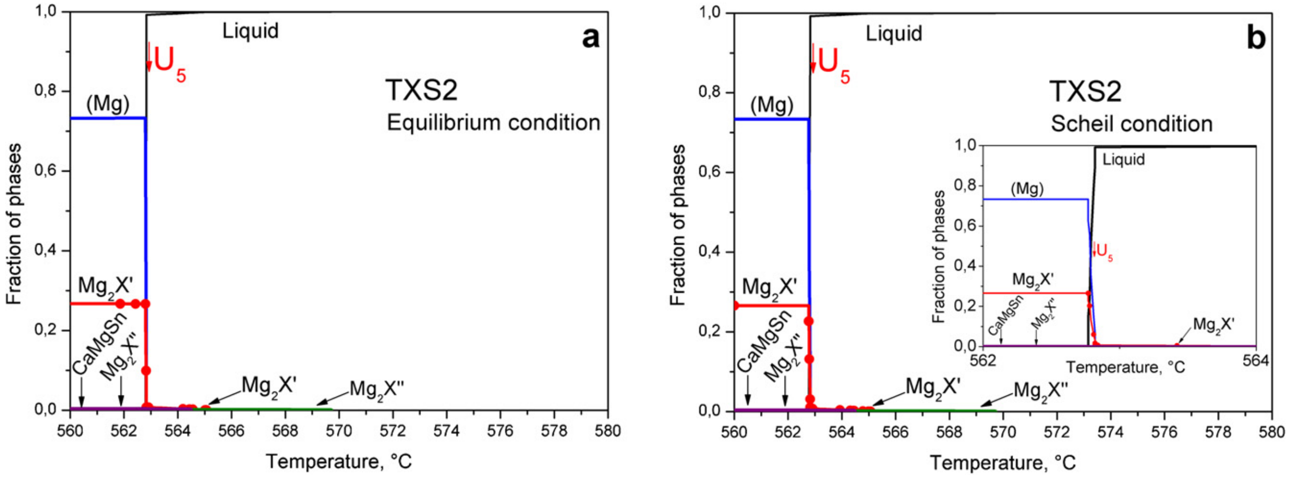

Fig. 13. Phase amounts for sample TXS2, see Fig. 11, calculated for solidification under (a) equilibrium and (b) Scheil conditions.

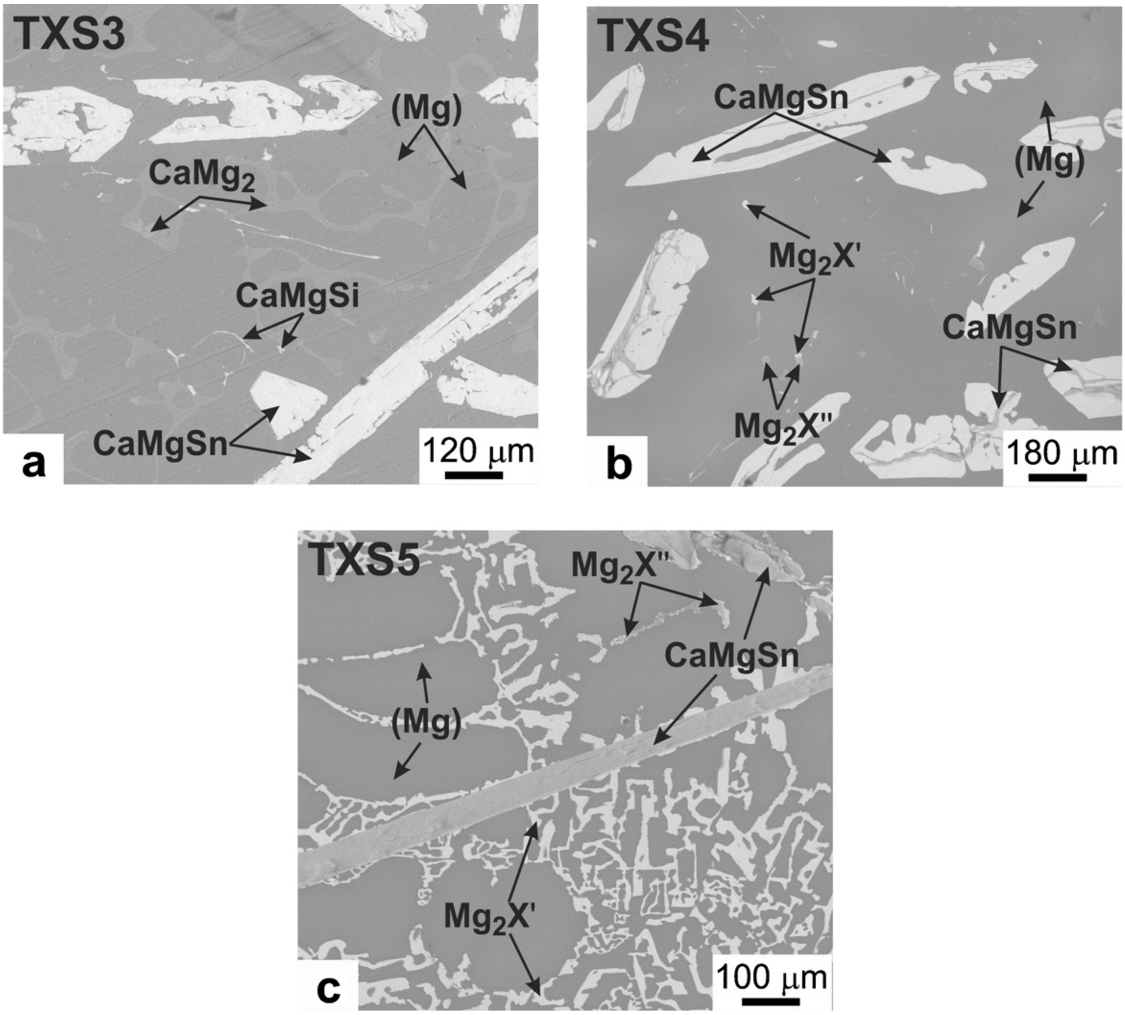

Fig. 15. Scanning electron micrographs (SEM/BSE) of sample (a) TXS3, (b) TXS4 and (c) TXS5 after slow cooling in DTA.

in Fig. 14. These are the transition-type reactions reaction U_4, L + CaMgSi = (Mg) + Mg_2X'' + CaMgSn, at 589.3 °C and U_5, L + Mg_2X'' = CaMgSn + (Mg) + Mg_2X' at 562.8 °C. Below this solidus a four-phase microstructure (Mg) + Mg_2X' + CaMgSn + Mg_2X'' with calculated phase fractions in qualitative agreement with the microstructure in Fig. 15c is observed. In the phase diagram section an additional solid state invariant reaction at 456.1 °C is given, (Mg) + CaMgSn + $Mg_2X'' \rightarrow Mg_2X'$ + CaMgSi. This transformation should, if equilibrating, essentially consume the Mg_2X'' and produce CaMgSi. However, no thermal signal at all is detected near that temperature and also the microstructure of TXS5 suggests that this solid state reaction does not occur at the cooling rate of the DTA experiment.

The thermal signals of sample TXS4 can be interpreted by reviewing the calculated enthalpy variation with temperature under both equilibrium and Scheil conditions in Fig. 16. We generally apply this procedure since it is better than the simple comparison with phase diagrams. The vertical arrows indicate calculated phase transition temperatures and superimposed are the experimental DSC/DTA signals using the same symbols as in the phase diagram, Fig. 14. In Fig. 16a the sequence of equilibrium phase regions is separated by dashed lines and it is noted that the invariant reactions (bold font) occur over a range of enthalpy values at constant temperature. By contrast, under Scheil conditions in Fig. 16b, also separated by dashed lines, only the phases actually precipitating from liquid in the temperature regions are listed. The invariant reactions U_4 and U_5 are given in brackets to indicate that the liquid only touches these five-phase equilibria but they do not proceed. Both reactions are of the transition-type, as detailed in Table 5, and under the Scheil conditions it is impossible to consume a solid phase.

The enthalpy curves in Fig. 16a and b reveal the strongest variation at 633 °C with beginning (Mg) crystallization, thus assigned to the strongest signal shown in Table 3. The subsequent reaction U_4 at 589.3 °C produces a much smaller enthalpy variation under equilibrium conditions and solidification terminates. Under Scheil conditions no enthalpy effect at all is seen and a significant fraction of residual liquid, $f_L = 0.14$, proceeds down to lower temperature hitting the reaction U_5 at562.8 °C. Even though this U-type reaction cannot proceed under Scheil conditions an enthalpy effect is calculated because of the transition of the residual liquid ($f_L = 0.09$) into the subsequent and final L → (Mg) + Mg_2X' + CaMgSn solidification step, terminating at 562.77 °C. In this narrow temperature range the Mg_2X' phase, non-equilibrium for this alloy, is produced. Both, the weak thermal signal at 564 °C and the occurrence of Mg_2X' in the microstructure, see Fig. 15b, support the interpretation that sample TXS4 solidifies close to Scheil conditions as opposed to equilibrium conditions.

After this discussion a remark should be made why, by contrast, for sample TXS5 the strong thermal signal at 603–600 °C in Table 3 was related to reaction U_4. First of all, the extent of reaction U_4 under equilibrium, and thus the enthalpy effect, is sig-

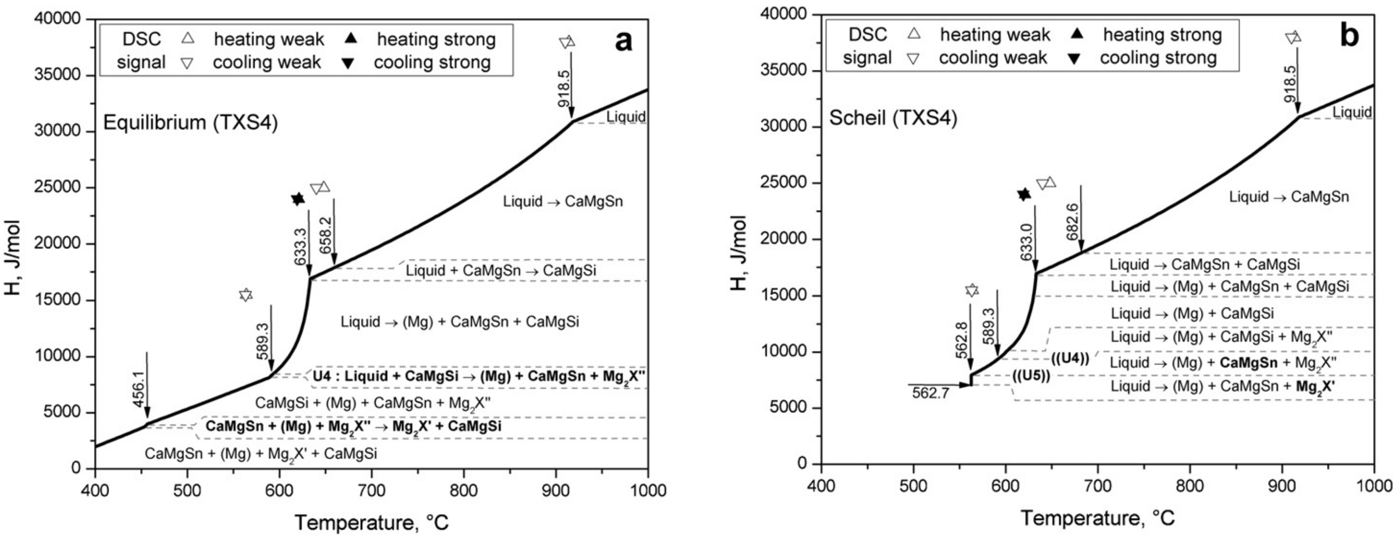

Fig. 16. Calculated enthalpy variation of sample TXS4 under (a) equilibrium and (b) Scheil conditions. The DSC signals display the experimental temperatures and are placed visually close (arbitrary enthalpy) to the calculated data to facilitate comparison with breaks in the enthalpy curve.

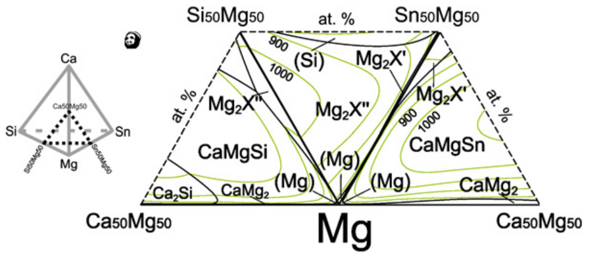

Fig. 17. Combination of the calculated ternary liquidus projections up to 50 at.% Mg from the three subsystems of the Mg–Ca–Si–Sn quaternary system.

nificantly larger for alloy TXS5 compared to TXS4. Second, a strong enthalpy variation is calculated for the start of (Mg) crystallization at 604.1 °C (equilibrium) or 603.5 °C (Scheil). This would fit the strong signal even better than U_4 (equilibrium), however, because of the narrow temperature range, a unique assignment to these three possible effects is difficult and some overlap may be considered. Similarly, the last strong signal of TXS5 at 565–563 °C may be assigned either to U_5 (equilibrium) at 562.8 °C or, under Scheil conditions, to freezing of residual liquid ($f_L = 0.39$) into the subsequent and final L → (Mg) + Mg_2X' + CaMgSn solidification step, terminating at 562.77 °C.

4.3. Quaternary Mg–Ca–Si–Sn phase diagram

The calculated partial liquidus surface of the Mg–Ca–Si–Sn quaternary system is presented in Fig. 17 as combination of the liquidus projections of the ternary edge systems for compositions 50–100 at.% Mg. A tetrahedron comprising quaternary alloy compositions, depicted in the insert, is formed by folding the Ca-containing ternaries up, thus forming a top vertex at pure Ca. The invariant six phase reactions involving the liquid phase and (Mg) in Mg-corner are listed in Table 5. Some of these reactions degenerate almost to a ternary edge system, for example, especially the reaction U_6 at 515.4 °C involves a liquid phase composition of only 1×10^{-6} at.% Si and the transformed CaMgSi phase fraction is virtually zero (3.4441e-005). The temperature of this reaction is also virtually identical to that of the E_3 reaction in the Mg–Sn–Ca system investigated by Kozlov et al. [11]. Thus, in reality, U_6 degenerates to this ternary eutectic reaction, L = CaMgSn + (Mg) + $CaMg_2$.

The combination of the ternary liquidus surfaces in Fig. 17 provides an overview of the relatively narrow extent of primary crystallization of (Mg), beyond which primary intermetallic precipitates are expected in the quaternary system, namely $CaMg_2$, CaMgSi, Mg_2X'', Mg_2X' and CaMgSn. All these solid phases do have their origin in the binary or, in case of CaMgSi, ternary subsystems. However, solid solution ranges extend into quaternary compositions, as indicated by the sublattice models for CaMgSn, $(\mathbf{Ca},\mathbf{Mg})_1(\mathrm{Ca})_1(\mathbf{Sn},\mathrm{Si})_1$, and CaMgSi, $(\mathrm{Ca},\mathbf{Mg})_1(\mathbf{Ca})_1(\mathrm{Sn},\mathbf{Si})_1$, respectively, with majority species indicated by bold font. Ternary compositions are observed for Mg_2X'', $(\mathrm{Mg})_2(\mathbf{Si},\mathrm{Sn})_1$, and Mg_2X', $(\mathrm{Mg})_2(\mathbf{Sn},\mathrm{Si})_1$, while only $CaMg_2$ remains a stoichiometric phase in the quaternary system. All these solubilities were determined by EDX analysis of quaternary samples as stated above. Therefore, no separate (true) quaternary phase is observed and

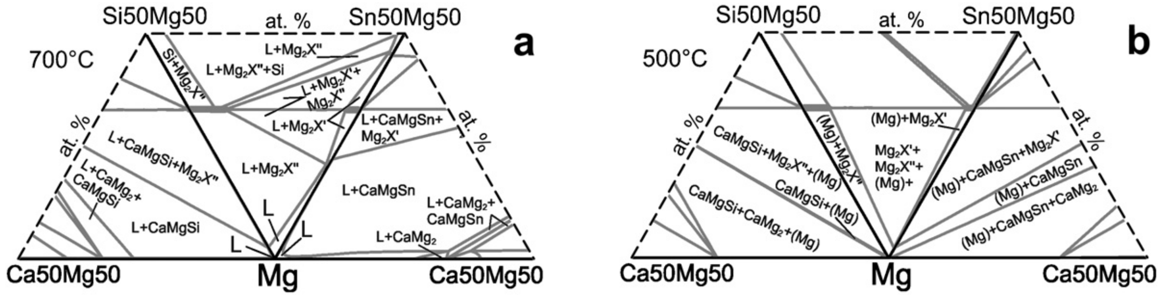

Fig. 18. Combination of the calculated ternary isothermal sections up to 50 at.% Mg at (a) 700 °C and (b) 500 °C from the three subsystems of the Mg–Ca–Si–Sn quaternary system.

this agrees with a general expectation for metallic systems [31].

In a similar fashion the combination of the ternary isothermal sections at 700 °C and 500 °C in Mg-corner are shown in Fig. 18a and b. Fig. 18a provides an overview of the narrow homogeneous region of liquid phase, extending from pure Mg at 700 °C essentially along the binary edges Mg–Ca, Mg–Sn and somewhat along Mg–Si. Five solid phases are in equilibrium with this liquid: $CaMg_2$, Mg_2X', Mg_2X'', CaMgSi and CaMgSn. The corresponding phase diagram at 500 °C shows the solid state equilibria in Fig. 18b. The same five solid intermetallic phases are now in equilibrium with the emerged solid (Mg) phase.

5. Conclusions

The viability of a procedure for the selection of multicomponent key samples [10] is demonstrated for the Mg–Ca–Si–Sn quaternary system. The corresponding experimental work is combined with the Calphad method to generate a consistent thermodynamic description of the Mg–Ca–Si–Sn quaternary system, validated for Mg-rich alloys.

The thermodynamic description and phase diagram of the ternary Mg–Si–Sn system, developed also in this work, deviates significantly from the literature [17]. The phase diagram proposed here is supported by dedicated DTA/DSC experiments and microstructure analysis on samples along the 66.67 at.% Mg section Mg_2X'–Mg_2X'' (Mg_2Sn–Mg_2Si) and the first experiment ever reported on a 90 at.% Mg sample. In addition to deviations along the Mg_2X'–Mg_2X'' section it is found that the primary crystallization field of (Mg) is significantly smaller compared to the previously suggested Mg–Si–Sn phase diagram [17].

Using the tool of thermodynamic equilibrium and Scheil calculations the solidification paths of ternary and quaternary alloys are analyzed in detail with respect to the precipitation sequence of phases and their amounts and it compares well with the actual phase formation in the microstructure. The most efficient comparison to the experimental thermal signals from DTA/DSC is done by calculation of the enthalpy variation with temperature, exemplified for one quaternary alloy.

It is also noted that for most of the Mg-rich alloys the effective phase formation and the thermal signals simulated by calculations under the extreme conditions of Scheil and equilibrium are quite similar. It may be suggested, in first approximation, that the different cooling rates associated to these conditions may produce similar effective phase formation in the Mg-rich Mg–Ca–Si–Sn alloys.

A thermodynamic description for the quaternary Mg–Ca–Si–Sn phase diagram, developed from the assessed ternary subsystems, is validated for alloys in equilibrium with (Mg). For the first time, the ternary/quaternary solid solubilities of pertinent intermetallic phases are quantitatively introduced and validated by experimental data.

Acknowledgment

This study is supported by the German Research Foundation (DFG) in the Priority Programme “DFG-SPP 1168: InnoMagTec”.

References

[1] I.-H. Jung, D.-H. Kang, W.-J. Park, N.J. Kim, S.H. Ahn, Int. J. Mater. Res. 98 (2007) 807–815.
[2] K.U. Kainer, Y. Huang, H. Dieringa, N. Hort, Mater. Sci. Forum 638–642 (2010) 73–80.
[3] Y.V.R.K. Prasad, K.P. Rao, N. Hort, K.U. Kainer, Int. J. Mater. Res. 101 (2010) 300–306.
[4] M.-B. Yang, L. Cheng, F.-S. Pan, Trans. Nonferrous Met. Soc. China 20 (2010) 584–589.
[5] D.-G. Kim, H.-T. Son, J.-S. Lee, Mater. Sci. Forum 620–622 (2009) 169–172.
[6] K.P. Rao, K. Suresh, N. Hort, K.U. Kainer, Mater. Sci. Forum 654–656 (2010) 635–638.
[7] L. Kaufman, H. Bernstein, Computer Calculation Of Phase Diagrams With Special Reference To Refractory Materials, Academic Press, New York, 1970.
[8] Y.A. Chang, S. Chen, F. Zhang, X.-Y. Yan, F.-Y. Xie, R. Schmid-Fetzer, Prog. Mater. Sci. 49 (2004) 313–345.
[9] H.L. Lukas, S.G. Fries, B. Sundman, Computational Thermodynamics: The Calphad Method, Cambridge University Press, 2007.
[10] A. Janz, J. Gröbner, R. Schmid-Fetzer, J. Phase Equilib. Diffusion 30 (2009) 157–175.
[11] A. Kozlov, M. Ohno, R. Arroyave, Z.K. Liu, R. Schmid-Fetzer, Intermetallics 16 (2008) 299–315.
[12] D. Kevorkov, R. Schmid-Fetzer, F. Zhang, J. Phase Equilib. Diffusion 25 (2004) 140–151.
[13] S. Fries, H.-L. Lukas, J. Chem. Phys. 90 (1993) 181–187.
[14] J. Gröbner, I. Chumak, R. Schmid-Fetzer, Intermetallics 11 (2003) 1065–1074.
[15] M. Ohno, A. Kozlov, R. Arroyave, Z.K. Liu, R. Schmid-Fetzer, Acta Mater. 54 (2006) 4939–4951.
[16] H.L. Lukas, in: I. Ansara, A.T. Dinsdale, M.H. Rand (Eds.), European Comm. EUR 18499 En, Luxembourg, 1998, pp. 264–265.
[17] I.-H. Jung, D.-H. Kang, W.-J. Park, N.J. Kim, S.H. Ahn, Calphad 31 (2007) 192–200.
[18] Sh.F. Muntyanu, E.B. Sokolov, E.S. Makarov, Inorg. Mater. 2 (1966) 740–744, translated from Izv. Akad. Nauk. SSSR, Neorg. Mater. 2 (1966) 870–875.
[19] E.N. Nikitin, E.N. Tkalenko, V.K. Zaitsev, A.I. Zaslavskii, A.K. Kuzentsov, Inorg. Mater. 4 (1968) 1656–1659, translated from Izv. Akad. Nauk SSSR, Neorgan. Mater. 4 (1968) 1902–1906.
[20] E.S. Makarov, Sh.F. Muntyanu, E.B. Sokolov, Inorg. Mater. 3 (1967) 290–293, translated from Izv. Akad. Nauk. SSSR, Neorg. Mater. 3 (1967) 329–332.
[21] E.N. Nikitin, V.G. Bazanov, V.L. Tarasov, Sov. Phys. – Solid State 3 (12) (1961) 2648–2651, translated from Fiz. Tverd. Tel. 3(12) (1961) 3645–3649.
[22] E.N. Nikitin, V.K. Zaitsev, Inorg. Mater. 2 (1966) 1698–1701, translated from Izv. Akad. Nauk SSSR, Neorg. Mater. 2 (1966) 1961–1965.
[23] R. Ferro, H. Flandorfer, B. Kasper, A. de Kroon in: G. Effenberg (Eds.), Ternary Evaluations, in *MSI Eureka,* Document ID: 10.27956.2.20, Materials Science International Services GmbH, Stuttgart, 2000.
[24] [24] D. Emadi, L.V. Whiting, R. Schmid-Fetzer, in: Hirsch, Skrotzki and Gottstein (Eds.) Aluminum Alloys–Their Physical and Mechanical Properties, Vol. 1, Published by Wiley-VCH GmbH&Co., Weinheim, Germany (IBSN # 978-3-527-32367-8), (2008) 328–335 Proceedings of the 11th International Conference on Aluminum Alloys, 22–26 Sept. 2008, Aachen, Germany.
[25] R. Schmid-Fetzer, Mater. Sci. Forum 618–619 (2009) 183–190.
[26] A.T. Dinsdale, Calphad 15 (1991) 317–425.
[27] O. Redlich, A.T. Kister, Ind. Eng. Chem. 40 (1948) 345–348.
[28] S.-L. Chen, S. Daniel, F. Zhang, Y.A. Chang, W.-A. Oates, R. Schmid-Fetzer, J. Phase Equilib. Diffusion 22 (2001) 373–378.
[29] W. Cao, S.-L. Chen, F. Zhang, K. Wu, Y. Yang, Y.-A. Chang, R. Schmid-Fetzer, W.-A. Oates, Calphad 33 (2009) 328–342.
[30] D. Mirkovič, R. Schmid-Fetzer, Z. Metallkd. 97 (2006) 119–129.
[31] U. Kattner, J. Mater. 49 (1997) 14–19.